



**University of  
Sunderland**

Jatti, Vijaykumar S., Saiyathibrahim, A., Murali Krishnan, R., Jatti, Ashwini V., Suganya Priyadharshini, G. and G. Mohan, Dhanesh (2024) Investigating the Effect of Volumetric Energy Density on Tensile Characteristics of As Built and Heat Treated AlSi10Mg Alloy Fabricated by Laser Powder Bed Fusion. *Advanced Engineering Materials*, 240192. p. 2401924. ISSN 1527-2648

Downloaded from: <http://sure.sunderland.ac.uk/id/eprint/18611/>

**Usage guidelines**

Please refer to the usage guidelines at

<http://sure.sunderland.ac.uk/policies.html> or alternatively contact [sure@sunderland.ac.uk](mailto:sure@sunderland.ac.uk).

# Investigating the Effect of Volumetric Energy Density on Tensile Characteristics of As-Built and Heat-Treated AlSi10Mg Alloy Fabricated by Laser Powder Bed Fusion

Vijaykumar S. Jatti, A. Saiyathibrahim, R. Murali Krishnan, Ashwini V. Jatti, G. Suganya Priyadharshini, and Dhanesh G. Mohan\*

Pore emergence during the laser powder bed fusion (LPBF) technique significantly impairs mechanical characteristics. Therefore, the elimination of pores is a pressing issue to ensure the quality and productivity of manufactured components. The objective of this study is to evaluate how certain parameters, such as laser power, layer thickness, exposure time, hatch distance, and volumetric energy density, affect the microstructure and tensile properties of AlSi10Mg specimens generated by LPBF in both their original state and after undergoing a solution heat treatment. The volumetric energy density (VED) is often used to optimize process parameters in the LPBF approach since it thoroughly evaluates all four main factors. This article specifically examines the impact of VED on the microstructural features and tensile characteristics of printed parts. The high VED of  $78.13 \text{ J mm}^{-3}$  decreases the occurrence of porosity and defects, hence enhancing the tensile characteristics of the specimens produced. Regarding specimens that have undergone solution heat treatment, the recommendation is to decrease the laser power to 350 W, which results in a VED of  $60.76 \text{ J mm}^{-3}$  and outstanding tensile characteristics. These findings provide fresh perspectives to achieve improved tensile properties of AlSi10Mg parts using LPBF processing settings.


## 1. Introduction

Additive manufacturing (AM) is a manufacturing method that enables the production of objects by sequentially printing layers, following the instructions of a digital 3D model.<sup>[1,2]</sup> This unique capability allows for the creation of complex forms that are almost impossible to achieve using conventional techniques. AM is a very important tool that enables designers to easily create unique and intricate models without the limitations usually seen in conventional production processes. These constraints include excessive material waste, challenges in creating complex shapes, and the requirement for specialized tools. Consequently, engineers have enhanced their capability to design freely by utilizing AM. Furthermore, the ability to produce components as needed enhances the speed of manufacturing, reduces the length of supply chains, minimizes storage

V. S. Jatti  
Department of Mechanical Engineering  
Symbiosis Institute of Technology, Symbiosis International  
(Deemed University)  
Pune 412115, India

V. S. Jatti  
Department of Mechanical Engineering  
School of Engineering and Applied Sciences  
Bennett University  
Greater Noida Uttar Pradesh 201310, India

A. Saiyathibrahim  
University Centre for Research and Development  
Chandigarh University  
Punjab 140 413, India

 The ORCID identification number(s) for the author(s) of this article can be found under <https://doi.org/10.1002/adem.202401924>.

© 2024 The Author(s). Advanced Engineering Materials published by Wiley-VCH GmbH. This is an open access article under the terms of the Creative Commons Attribution License, which permits use, distribution and reproduction in any medium, provided the original work is properly cited.

DOI: 10.1002/adem.202401924

R. Murali Krishnan  
Department of Mechanical Engineering  
Karpagam Institute of Technology  
Coimbatore 641 105, Tamil Nadu, India

A. V. Jatti  
Department of Instrumentation Engineering  
D Y Patil Institute of Technology  
Savitribai Phule Pune University  
Pune 411007, India

G. Suganya Priyadharshini  
Department of Mechanical Engineering  
Coimbatore Institute of Technology  
Coimbatore 641 014, Tamil Nadu, India

D. G. Mohan  
Faculty of Technology  
School of Engineering  
University of Sunderland  
Sunderland SRI 3SD, UK  
E-mail: dhanesh.mohan@sunderland.ac.uk

D. G. Mohan  
Centre of Research Impact and Outcome  
Chitkara University Institute of Engineering and Technology  
Chitkara University  
Punjab 140401, India

requirements, eliminates expenses associated with shipping, and decreases the time required to obtain essential replacement parts.<sup>[3]</sup> AM techniques are categorized into seven distinct groups according to the ISO/ASTM 529000:2015 standard: directed energy deposition (DED), material extrusion, material jetting, binder jetting, powder bed fusion (PBF), vat photopolymerization, and sheet lamination.<sup>[4]</sup> AM technologies have the potential to utilize a wide range of materials, such as polymers, ceramics, and metals. Researchers and companies are increasingly interested in metallic materials among these materials. Metal AM offers environmental benefits, including reduced waste, enhanced quality, lesser pollutant emissions, and the ability to produce parts as needed. All AM systems operate based on the same fundamental principle of constructing a structure by adding material to a substrate. However, the two most widely used commercial technologies for metal AM are DED and laser PBF (LPBF).<sup>[5,6]</sup> LPBF is an AM technique that uses powerful lasers to completely melt metal powder and produce objects that closely resemble the desired form. This method has many key benefits, including the ability to produce complex, topology-optimized structures with minimum waste and no need for tools. Additionally, it enables substantial customization and design flexibility.<sup>[5,7]</sup> LPBF printers are the most commonly found systems in the market because of their exceptional resolution, typically ranging between 10 and 50  $\mu\text{m}$  for each layer. In contrast, powder-fed DED printers have a layer thickness of  $\approx 250 \mu\text{m}$ .<sup>[8]</sup> Interestingly, BMW is the pioneering Original Equipment Manufacturer that utilizes the LPBF technique to manufacture aluminum alloy-based component in large quantities for the latest i8 Roadster.<sup>[9]</sup> Parallelization and boosting scanning speed, laser power, and layer thickness are effective methods for enhancing the efficiency of LPBF.<sup>[10–12]</sup> The utilization of a high-power laser can facilitate the extension of LPBF processing to alloys like copper and aluminum, which possess strong thermal conductive properties and minimal absorptivity.<sup>[13,14]</sup> LPBF process has an exceptionally high cooling rate of around  $106 \text{ K s}^{-1}$ , which is significantly higher than the maximum cooling rate of  $\approx 103 \text{ K s}^{-1}$  in traditional casting processes. As a consequence, the outcome is the creation of aluminum goods characterized by a refined solidification microstructure. These items have a relatively high level of strength and have the capacity to become harder when subjected to stress in their as-built state.<sup>[15–18]</sup>

Owing to its favorable characteristics of low density, high specific strength, great corrosion resistance, and superior melt fluidity, aluminum alloy has emerged as an optimal structural and functional material in aircraft, armaments, and many other fields.<sup>[19–22]</sup> Hypo- and near-eutectic Al–Si alloys, such as AlSi10Mg, are widely used in the aviation and automotive sectors because of their exceptional weldability and castability. As a result, these alloys are increasingly being recognized for their potential in LPBF processing.<sup>[23–25]</sup> The AlSi10Mg alloy treated via LPBF has been extensively studied for its potential use in the automotive and aerospace sectors. This is mostly owing to its excellent castability, remarkable resistance to corrosion, and favorable weldability. Additionally, it exhibits an excellent mechanical characteristic to density ratio.<sup>[26]</sup> Nevertheless, prior research indicates three primary obstacles that impede the extensive adoption of aluminum alloys in LPBF technology: the powder exhibits 1) poor flowability and low apparent density,

2) strong thermal conductivity, and 3) contains a native  $\text{Al}_2\text{O}_3$  scale.<sup>[23,27,28]</sup> Significant attempts have been undertaken to overcome these challenges by concentrating on enhancing the operational parameters for laser units with high power.<sup>[29,30]</sup> Furthermore, the as-built AlSi10Mg LPBF specimens exhibited higher mechanical features in comparison to specimens produced by conventional casting procedures.<sup>[31,32]</sup> Liu et al.<sup>[33]</sup> reported that AlSi10Mg parts produced via LPBF exhibit mechanical properties, including hardness, ultimate tensile strength (UTS), elongation and impact energy that are either higher or at least equivalent to those of cast AlSi10Mg components. This is attributed to the presence of an extremely fine microstructure and a well-distributed Si phase.<sup>[33]</sup> Gandolfi et al.<sup>[34]</sup> proposed that the AlSi10Mg parts have outstanding tensile properties (yield strength [YS] of 142 MPa, elongation of 5%, and UTS of 220 MPa), especially when the microstructure is more refined.<sup>[34]</sup> Hirata et al.<sup>[35]</sup> and Limbasiya et al.<sup>[36]</sup> confirmed that the tensile strength of AlSi10Mg produced using LPBF is greater than that of the die cast version. However, the die cast counterpart exhibits superior ductility.<sup>[35,36]</sup>

Conventionally cast Al–Si alloys have large, needle-shaped silicon and precipitates that contain magnesium. The presence of big silicon-rich precipitates has a negative impact on the ductility of the material and hence it is necessary to refine them.<sup>[37]</sup> Prior research has shown that the LPBF technology may be used to improve the microstructure of the AlSi10Mg alloy, resulting in increased mechanical strength. This improvement is attributed to the technology's ability to rapidly cool the alloy.<sup>[38,39]</sup> The microstructure of AlSi10Mg developed by the LPBF technique revealed notable distinctions compared to the microstructure of the as-cast AlSi10Mg. The rapid solidification caused by LPBF leads to the formation of a considerable fine structure consisting of an  $\alpha$ -Al matrix with a cellular-dendritic microstructure and very tiny fibrous Si.<sup>[40]</sup> Attaining full density in end products is a highly sought-after objective in AM. This is because even the presence of small amounts of residual porosity significantly diminishes mechanical properties. Consequently, there is a wealth of experimental data in the literature dedicated to density in AM.<sup>[41,42]</sup> It needs to be noted that regarding to the current state of science near-full dense parts with a relative density of nearly 99.8% are feasible with LPBF technology.<sup>[43]</sup> Upon examining the influence of process parameters on LPBFed AlSi10Mg, it was shown that a higher scanning speed is the most efficient method for achieving enhanced dimensional accuracy, reduced surface roughness, and improved part density.<sup>[44]</sup> Riener et al.<sup>[45]</sup> identified that increasing scanning speeds lead to reduced part density. Moreover, the use of powders with smaller particle sizes results in consistently reduced densities of the parts, whereas employing powders with a more spherical shape can lead to higher part densities.<sup>[45]</sup> AM typically occurs at near-full density up to 99.8% and the parameters of scanning speed, and powder quality can enhance the density and the performance of the part.<sup>[46]</sup> Volumetric energy density (VED) in LPBF influences part density; elevated VED delivers adequate energy to completely melt the powder, yielding denser components. Enhancing VED reduces faults such as porosity, hence augmenting the mechanical qualities of the manufactured component. The fabrication of dense components by LPBF guarantees enhanced mechanical qualities and minimizes flaws, such as

porosity, that may affect part performance. Dense components additionally improve durability and load-bearing capacity in essential applications.<sup>[47]</sup> The importance of VED in the analysis of components produced by LPBF is currently growing. The mechanical properties of additively built components, including surface roughness, hardness, pore count, and size, may be analyzed in relation to VED. This understanding can assist designers in managing multiple process parameters simultaneously.<sup>[48]</sup> Giovagnoli et al.<sup>[49]</sup> reported that VEDs of 30–110 J mm<sup>-3</sup> were determined to be appropriate for producing fully dense components (relative density of 98–99.9%), with most data concentrated between 40 and 70 J mm<sup>-3</sup>.<sup>[49]</sup> Singla et al.<sup>[50]</sup> analyzed the printability of Ti–6Al–4V alloy by using VED. The results showed a clear correlation between VED values and the presence of internal porosity in the final components. This indicates that it is possible to decrease the remaining porosity by applying material within a designated VED range. Inadequate energy input to the powder bed leads to adverse melting conditions, resulting in the formation of a substantial number of big holes in the final components, ranging in size from tens to hundreds of microns. The presence of these pores has detrimental effects on mechanical properties, such as tensile strength and fatigue resistance. Once the energy density is beyond a certain threshold, a deposition scenario known as “keyhole mode” is attained. During this phase, the depth of the melt pool increases significantly, leading to the remelting of many layers. As a result of the significant energy concentration, the temperatures required for metals to boil are achieved, leading to the vaporization of the alloy. Moreover, the molten pool may experience a powerful internal Marangoni flow, which can result in the entrapment of gas bubbles driven by vapor. This, in turn, leads to an elevation in the porosity of the component.<sup>[50]</sup> Garcia-Cabezon et al.<sup>[51]</sup> examined the impact of the laser power and scanning approach, employing VED, on the microstructure and texture of LPBFed SS316L components. They revealed that the VED had a significant influence on both the microstructure and the quantity of the ferrite phase. VED is a valuable statistic for calculating the amount of energy supplied per unit volume of a powder bed in AM. It considers variables such as laser intensity, scanning velocity, and layer depth. By utilizing the VED, one can effectively select parameters that would result in the highest density of the printed object.<sup>[52]</sup>

Components produced with metal AM may need specific heat treatments to mitigate the residual stresses arising from manufacturing. The specimen may possess several forms of residual stresses during its construction. The experienced strain of the printed part restricts its use in its current condition. A significant amount of research has focused on heat treatments using two different methods: the first method involves using the standard heat treatments typically used for cast materials with the same compositions. In contrast, the second method involves optimizing the conditions of the heat treatment (such as temperature and duration) and examining the impacts of these conditions on both the microstructure and mechanical properties.<sup>[53]</sup> In the case of AlSi10Mg components manufactured via LPBF, silicon is mostly dissolved inside the aluminum matrix before undergoing heat treatment, which is different from cast parts. The annealing cycle promotes the system’s movement toward thermodynamic equilibrium, hence reducing any residual stresses that may occur throughout the LPBF process. These stresses have

the potential to induce distortions or microcracks. While annealing is often used to increase the malleability of alloys, the strengthening of alloys is accomplished by a precipitation-hardening process. Strengthening is achieved by undergoing a series of steps, including solution heat treatment, quenching, and artificial aging. This process results in the creation of intermetallic compounds from the unstable and too saturated solid solution of alloying elements in aluminum. The length of the solution and aging approaches is of utmost importance. It is important to prevent under-ageing and over-ageing as they might lead to a drop in hardness and a reduction in mechanical qualities.<sup>[42]</sup>

The limited understanding of the relationship between the technique, microstructure, and characteristics is especially apparent in the thermal postprocessing of components manufactured by LPBF. Heat treatments for metals manufactured via LPBF are often performed without meticulous attention, often relying on traditional processing techniques. An example of a frequent yet misguided technique is the use of T6 heat treatment for LPBF-processed AlSi10Mg. Due to the inherent disparity in microstructure resulting from LPBF processing versus traditional processing, it is unreasonable to anticipate equivalent changes in these microstructures after heat treatment. As a result, the heat treatments commonly used for LPBF-processed alloys are generally not ideal and might lead to lower mechanical qualities compared to parts treated using conventional methods. Hence, the requirement for customized heat treatments for metals treated with LPBF contributes to the difficulties in achieving maturity in metal AM. Subsequent to the T6 heat treatment, the hardness, YS, and UTS experienced a decrease of up to 20%, while the compressive strength was reduced by 56%. On the contrary, ductility was enhanced up to 4 times. Therefore, they proved that subjecting AlSi10Mg specimens generated using the LPBF technique to T6 heat treatments does not result in any increase in strength.<sup>[36]</sup> Cabrini et al.<sup>[54]</sup> discovered that subjecting materials to high temperature heat treatments at 400 and 500 °C resulted in a significant reduction in hardness. However, these treatments effectively avoided the occurrence of selective corrosion attack. Heat treatments conducted at temperatures of 200 and 300 °C for a duration of 2 h preserved the distinctive macrostructure of the melt pool. At elevated temperatures, the microstructure exhibited  $\alpha$ -Al matrix including spherical silicon particles. The size of these particles increased as the heat treatment temperature increased. To prevent the need for stress relieving heat treatments, it is recommended to employ a high building platform temperature, specifically up to 200 °C.<sup>[54]</sup> Liu et al.<sup>[55]</sup> found that subjecting the specimens to annealing at a temperature of 300 °C resulted in a change in hardness at various sites within the lattice specimen. At a high temperature of 530 °C, a uniform microstructure was created, resulting in consistent hardness throughout all areas. The standardization of mechanical characteristics in the lattice specimens has been achieved at this temperature.

Within the framework of LPBF, there are four specific factors that are linked to alloy processing. The parameters consist of the scan speed (mm s<sup>-1</sup>), the laser power (W), the distance between successive laser scans, sometimes referred to as hatch spacing (mm), and the thickness of the powder layer (mm).<sup>[56]</sup> According to Wu et al.<sup>[39]</sup> hatch spacings less than 0.1 mm resulted in the lowest porosity, whereas a maximum density

of  $100 \text{ J mm}^{-3}$  achieved high density. The porosity of AlSi10Mg components in LPBF has an impact on their mechanical properties and overall quality. To effectively manage the quality of components, it is necessary to understand and control the relationship between porosity and VED in LPBF.<sup>[39,57]</sup> Dong et al.<sup>[58]</sup> investigated the effect of varying hatch spacing (0.05, 0.06, and 0.07 mm) and using two different laser strengths (150 and 180 W). They discovered that the maximum density was consistently achieved at an energy density of  $90 \text{ J mm}^{-3}$ , independent of the laser power used.<sup>[58]</sup> Hyer et al.<sup>[25]</sup> have studied the effect of LPBF processing parameters for AlSi10Mg alloy with the variation of laser power, scan speed, hatch spacing, and slice thickness. The deviation in the hatch spacing was found to have a very minor effect on relative density with a relative density greater than 99% realized at 250 W and 0.13 mm hatch spacing. During low scan speeds, the microstructure contained gas trapped pores and at high scan speeds lack of fusion flaws were observed. A processing window of  $32\text{--}54 \text{ J mm}^{-3}$  at scan speeds of  $1200\text{--}2000 \text{ mm s}^{-1}$  was found where high densities of defects were observed while the hardness of around 114–120 VHN.<sup>[25]</sup> All of the previously listed studies help to varying extents in understanding the influence of various LPBF settings on microstructural and mechanical characteristics. The presence of pores in LPBFed parts is directly affected by the volumetric energy density, which refers to the amount of energy input per unit volume during the LPBF process. Additionally, investigating the impact of VED on the tensile properties of AlSi10Mg alloy produced through LPBF entails examining how varying levels of energy input during the printing process influence the mechanical characteristics of the alloy, particularly its tensile properties.<sup>[59]</sup> The mechanical performance of LPBF components may be accurately evaluated by considering key tensile parameters such as UTS, YS, elongation, and ductility. The correlation between VED and tensile characteristics is intricate. Optimal VED may lead to enhanced mechanical characteristics by facilitating the formation of a more refined microstructure with reduced flaws and enhanced interlayer bonding. The novelty is in exploring a variety of VED configurations that have not been thoroughly examined in the current body of research. One such approach is to investigate both high and low VED regimes in order to determine the limits at which tensile qualities are maximized. This article presents a concise study that examines the effect of volumetric energy density on the tensile characteristics of heat-treated AlSi10Mg components. Therefore, it is considered crucial to execute methodical experiments and analyze samples using metallographic analysis and tensile testing in order to establish a correlation between microstructural characteristics and mechanical performance. The acquired insights may be used to develop process optimization techniques for LPBF of AlSi10Mg alloy, which might possibly improve its applicability for automotive, aerospace, and biomedical applications.

Nevertheless, to acquire a more thorough understanding of the influence of VED on the microstructural and tensile properties of LPBFed AlSi10Mg, this study was conducted. The processing variables, such as exposure time, laser power, layer thickness, and hatch distance, were considered and their collective impact during fabrication was correlated with VED. Instead of the linear energy density, the volumetric energy density was considered due to the fact that, when the layer thickness is constant, it is very useful to determine the effects of processing parameters on material properties without being obscured by changes in layer thickness. LPBF exposure time influences AM quality, resolution, surface texture, mechanical characteristics, and efficiency. It takes rigorous optimization and modification depending on the material, component shape, and intended output to enable consistent and high-quality part manufacture. In addition, components made from AlSi10Mg using LPBF were subjected to a solution heat treatment at a temperature of  $530 \text{ }^\circ\text{C}$  for a duration of 6 h. They were then rapidly cooled in order to reduce any residual stresses, make the microstructure uniform, improve mechanical properties, maintain dimensional stability, and ensure consistent performance. Optimizing additively generated AlSi10Mg component material properties and determining property changes while relating them to observed optical microstructures is critical. In this work, scanning electron microscopy (SEM) was used to analyze the tensile fracture mechanism found in AlSi10Mg specimens manufactured utilizing the LPBF technique.

## 2. Experimental Section

The AlSi10Mg powder utilized in this work was supplied by Sandvik Osprey, Neath, UK, and synthesized using gas atomization having a regular spherical shape with an average grain size about  $45 \mu\text{m}$ . AlSi10Mg powder composition used during the present investigation is presented in **Table 1**. Each of the specimens employed in the investigations was fabricated utilizing a Renishaw RenAM 500E LPBF equipment (Amison Engineering, Pune, India), which has a 500 W maximum laser beam power and an  $80 \mu\text{m}$  beam diameter. The printer has a build envelope of  $245 \times 245 \times 335 \text{ mm}$  and a build volume of 20.11 L. All LPBF experiment was conducted using the pulsed laser mode with the scan direction rotated by  $67^\circ$  for each succeeding layer with 5 mm stripe width and build platform preheating was not employed. **Table 2** displays variable process parameters that were employed in the specimen fabrication and designations of specimens are also given. In order to minimize oxidation, the construction chamber had been filled with extremely pure ( $>99.999\%$ ) argon gas after vacuuming to a pressure equal to 900 mbar. Previous to powering up the laser, the process was repeated 3 times to bring down the oxygen level to a value lower than 20 parts per million. After that, argon was injected into the chamber at a pressure  $\approx 20 \text{ mbar}$  more than

**Table 1.** AlSi10Mg powder composition.

Element	Si	Cu	Fe	Ni	Zn	Mg	Mn	Pb	Sn	Ti	Al
Composition [wt%]	10.8	0.05	0.55	0.05	0.10	0.35	0.45	0.05	0.05	0.15	Balance



**Table 2.** LPBF processing parameters used and their respective volumetric energy density.

Sr. nos.	Designation	Laser power [W]	Exposure time [ $\mu$ s]	Hatch distance [mm]	Layer thickness [mm]	Average density [ $\text{g mm}^{-3}$ ]	Relative density [%]	Volumetric energy density [ $\text{J mm}^{-3}$ ]
1	A	350	50	0.08	0.06	2.60055	97.03	60.76
2	B	350	45	0.09		2.60275	97.12	48.61
3	C	350	40	0.12		2.5843	96.43	32.41
4	D	450	50	0.08		2.58585	96.49	78.13
5	E	450	45	0.09		2.57965	96.26	62.50
6	F	450	40	0.12		2.5883	96.58	41.67
7	G	500	50	0.08		2.5672	95.79	86.81
8	H	500	45	0.09		2.5672	95.27	69.44
9	I	500	40	0.12		2.5715	95.95	46.30

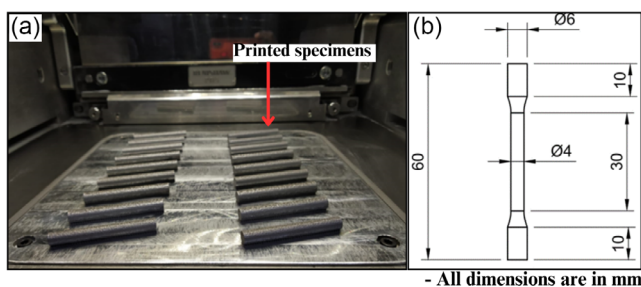


**Figure 1.** a) Specimens printed using LPBF process and b) schematic of tensile test specimen.

the ambient pressure. **Figure 1a** shows the specimen printing using LPBF process of diameter 6 and 60 mm length. Additionally, a batch of specimens was solution treated at 530 °C for 6 h, followed by quenching.

### 2.1. Volumetric Energy Density Calculation

The volumetric energy densities attained on every specimen with different process parameters are described in Table 2. For the purpose of providing a strong experimentation, Taguchi L9 orthogonal array was employed in the current study. The features of Taguchi methods include higher superiority to a variation, simple and efficient approach to experimenting, and a primary concern for loss functions in terms of quality. They are more easily interpreted, require fewer response functions, and could be even less expensive since the number of experimental runs is limited. Taguchi methods are also useful when the responses are nonlinear and unlike traditional optimization techniques consider both product and process characteristics simultaneously. Consequently, the advantages provided by Taguchi are particularly attractive to industries prioritizing quality and reliability. In order to enhance the performance of VED with regard to material characteristics and printing, it is necessary to fine-tune the laser power, scan speed, layer thickness, and laser spot size. Different materials may need variable VEDs to achieve optimal printing quality and mechanical properties. Supervising and controlling VED guarantees the quality and

performance of LPBF components. The computation and optimization of VED enhances the process control, quality of components, mechanical properties, and efficiency of AM for AlSi10Mg parts using LPBF. Volumetric energy density ( $\text{J mm}^{-3}$ ) is calculated as per Equation (1):<sup>[60]</sup>

$$\text{VED} = \frac{P}{\frac{\text{PD}}{E} \times d \times t} \quad (1)$$

where  $P$  is the laser power in watt,  $E$  is the exposure duration in  $\mu$ s,  $\text{PD}$  is the point distance in mm,  $d$  is the hatch spacing in mm, and  $t$  is the layer thickness in mm.

### 2.2. Microstructural Observation

The specific characteristics of a manufactured part are primarily influenced by the microstructure inside the deposited layers.<sup>[61]</sup> The microstructure of a material is affected by its solidification rate, which, in turn, influences physical and mechanical properties.<sup>[62]</sup> In relation to the analysis of phases and observations of microstructure for the specified materials, specimen preparation was performed. After using a polisher to refine the surface with grit sizes ranging from #400 to #4000, a 1  $\mu$ m diamond paste was used to create a 0.04  $\mu$ m colloidal silica. X-ray diffraction (XRD) was used to investigate the phases in the as-built LPBFed AlSi10Mg. The Bragg–Brentano geometry and a continuous scan mode of 10° min<sup>-1</sup> were employed. The analysis was performed using an Empyrean Series III Diffractometer with a customized phase composition range of 20–90°. A Cu anticathode was used at 35 kV and 40 mA. The samples, in their original state and after undergoing heat treatment, were etched using Keller's reagent, which consists of 95 mL of distilled water, 2.5 mL of HNO<sub>3</sub>, 1.5 mL of HCl, and 1 mL of HF. The etching process lasted for 30 s and was done to reveal the microstructure. The microstructure analysis follows the evaluation procedure outlined in ASM Handbook Vol 9:2004. The microstructure of LPBF printed AlSi10Mg components was first characterized and assessed using an optical microscope (OM), namely, the Nikon MA100 Inverted Metallurgical Microscope. The surface morphology and quality of the produced samples were assessed using JEOL In-Touch Scope JSM-IT200, an SEM technique.

### 2.3. Tensile Testing

The process of conducting a tensile test on an AlSi10Mg part is applying axial tension to the material until it reaches its UTS and fractures. This test assesses the mechanical properties of the material, such as its UTS, YS, and elongation at the point of failure. During the test, the AlSi10Mg component is securely fastened at both ends while a carefully controlled force is exerted. This force is steadily increased, causing the specimen to stretch until it eventually breaks. The obtained data offer significant insights into the behavior of the material when subjected to strain, which is essential for assessing its appropriateness for different applications, especially in industries such as aerospace and automotive where there is a need for lightweight, high-strength materials. To ascertain the tensile properties of items in their original state and after undergoing heat treatment. Tensile specimens were fabricated from printed bars in accordance with the ASTM E83-02 standard, as shown in Figure 1b. The tensile tests were conducted utilizing computerized servohydraulic digital universal testing equipment. The equipment was run at an extension rate of  $0.5 \text{ mm min}^{-1}$  while maintaining the ambient temperature.

## 3. Results and Discussion

The influence of volumetric energy density on the tensile strength of AlSi10Mg specimen, commonly used in AM processes like LPBF, is multifaceted. In LPBF, the VED influences the microstructure and porosity of the printed parts, which, in turn, affects their mechanical properties. Higher VEDs can lead to faster melting and solidification rates, potentially resulting in finer microstructures with reduced porosity, which could enhance the tensile strength of the alloy. However, excessive energy density can also induce defects like balling, keyholing, or excessive vaporization, leading to decreased tensile strength due to increased porosity or altered grain morphology. Therefore, optimizing the energy density parameters in the LPBF process for AlSi10Mg alloy is crucial to achieve the desired balance between energy absorption, microstructural refinement, and porosity control, ultimately influencing the tensile strength of the fabricated components.

### 3.1. Influence of Process Variables on Volumetric Energy Density

Table 2 illustrates the various process parameters used in the fabrication of the specimens. Furthermore, it demonstrates how these factors affect the VED and relative density of the AlSi10Mg specimens produced by LPBF while maintaining a consistent layer thickness of 0.06 mm. An asymmetrical distribution of relative density is seen as the laser power rises for components with varying exposure duration and hatch distance. The volumetric energy density is determined to be  $60.76 \text{ J mm}^{-3}$  when a laser power of 350 W is used, with an exposure duration of  $50 \mu\text{s}$  and a hatch distance of 0.08 mm. Increasing the laser power results in a greater quantity of energy being transferred to the powder bed within a given time frame. Higher laser power leads to a greater VED since it provides more energy to melt and

fuse the powder particles in a certain volume. Additionally, the relative density reaches its maximum value of 97.03%. By decreasing the exposure period to  $40 \mu\text{s}$  and the hatch distance to 0.12 mm, the VED can be reduced to as low as  $32.41 \text{ J mm}^{-3}$ . At a laser power of 500 W, the exposure period is  $50 \mu\text{s}$ , and the hatch distance is 0.08 mm, the volumetric energy density reaches its maximum value of  $86.81 \text{ J mm}^{-3}$ , while the relative density reaches its minimum value of 95.79%. The volumetric relative density shows a tendency to grow when the laser power, minimal hatch distance, and exposure time increase simultaneously. Similarly, when the laser power is fixed, reducing the exposure time and increasing the hatch distance also led to an increase in relative density and subsequently the volumetric relative density experiences a substantial decrease.<sup>[63]</sup> It is also observed that closer hatch distances increase the overlap and thus the energy deposition per unit volume, contributing to higher VED. Thinner layers required less energy to melt, leading to higher energy density for a given laser power and scanning speed. This is because the same amount of energy is spread over a smaller volume. Optimizing these factors is crucial for attaining the necessary quality and mechanical qualities of AlSi10Mg components in LPBF. By carefully considering these criteria, it is possible to achieve an energy density that is enough for fully melting and fusing powder particles while also reducing the occurrence of flaws such as porosity. Manufacturers may achieve consistent and dependable manufacturing of high-quality components by using advanced process monitoring and control systems to optimize these factors.

### 3.2. Microstructural Observation

The microstructure and pore features of the AlSi10Mg specimens produced by LPBF technique have a significant impact on their mechanical properties, namely, the tensile behavior. Typically, the LPBF specimens have a microstructure that is defined by a compact cellular-dendritic solidification pattern. This pattern consists of smaller main aluminum cells and a silicon network structure located between the cells. The primary parameters influencing the strengthening processes in LPBFed AlSi10Mg specimens are the cell size of the aluminum cells, rather than the grain size.<sup>[64]</sup> The presence of the silicon phase at the border of the aluminum cells effectively prevents the movement of dislocations. The Orowan bypassing process, produced by the Si network topology, enhances the mechanical characteristics.<sup>[65]</sup> **Figure 2** displays the distinctive features found in optical micrographs of as-built LPBFed specimens that were printed using various combinations of process configurations. Similarly, **Figure 3** depicts the exceptional features seen in optical micrographs of heat-treated LPBF specimens produced with different combinations of process configurations. Upon examination of the as-built specimens, it is obvious that there is a large quantity of pores present; however, the size of these pores is relatively small. As the VED increases, the overall quantity of pores decreases; meanwhile, the size of pores simultaneously increases. Previous research investigations have demonstrated that porosity has an impact on the mechanical strength, fatigue strength, and elongation to rupture. It is well known that all powder-based procedures inherently possess certain porosity



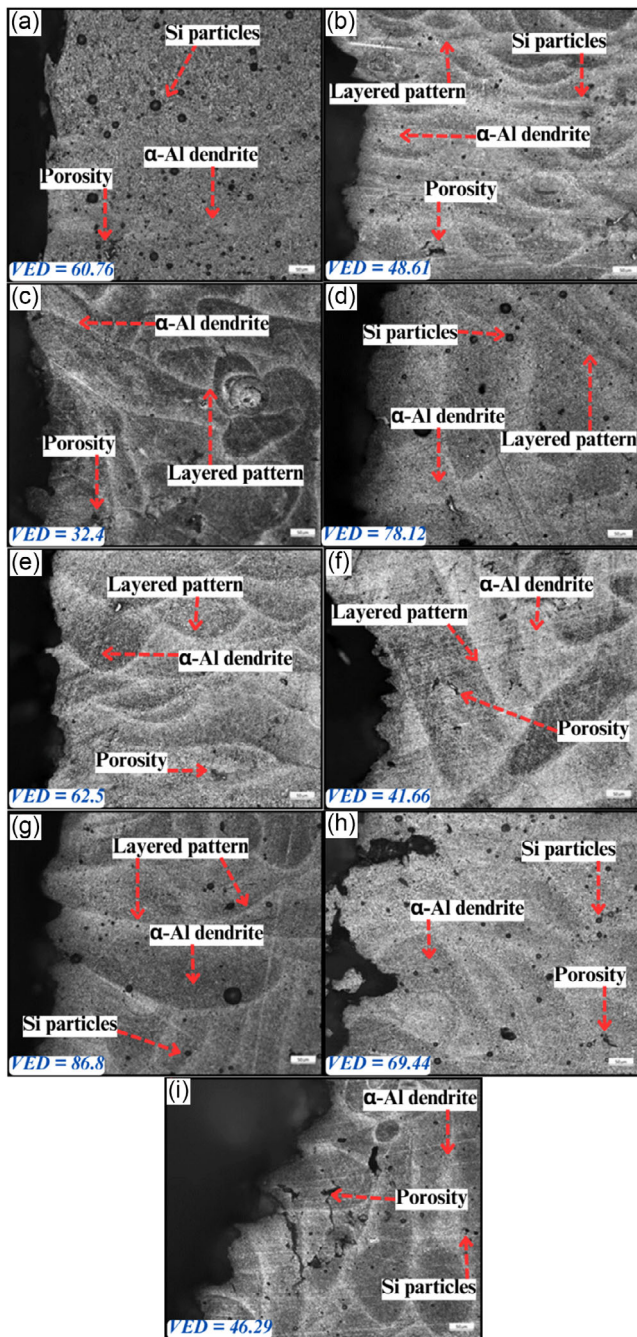


**Figure 2.** a–i) Optical micrographs of as-built LPBFed specimens printed using various process parameters combinations.

caused by internal pores inside the initial powder particles,<sup>[66]</sup> Thus, it is essential to determine the density of the as-built parts in order to precisely evaluate its mechanical properties.<sup>[67]</sup> The presence of larger pores is attributed to a lack of appropriate linear energy density, which leads to the occurrence of an unfused phenomena and the development of unmelted regions inside the specimen/part. Exposure of the powder to radiation results in an inadequate liquid phase that cannot fully fill the available space. This causes the formation of big pores with

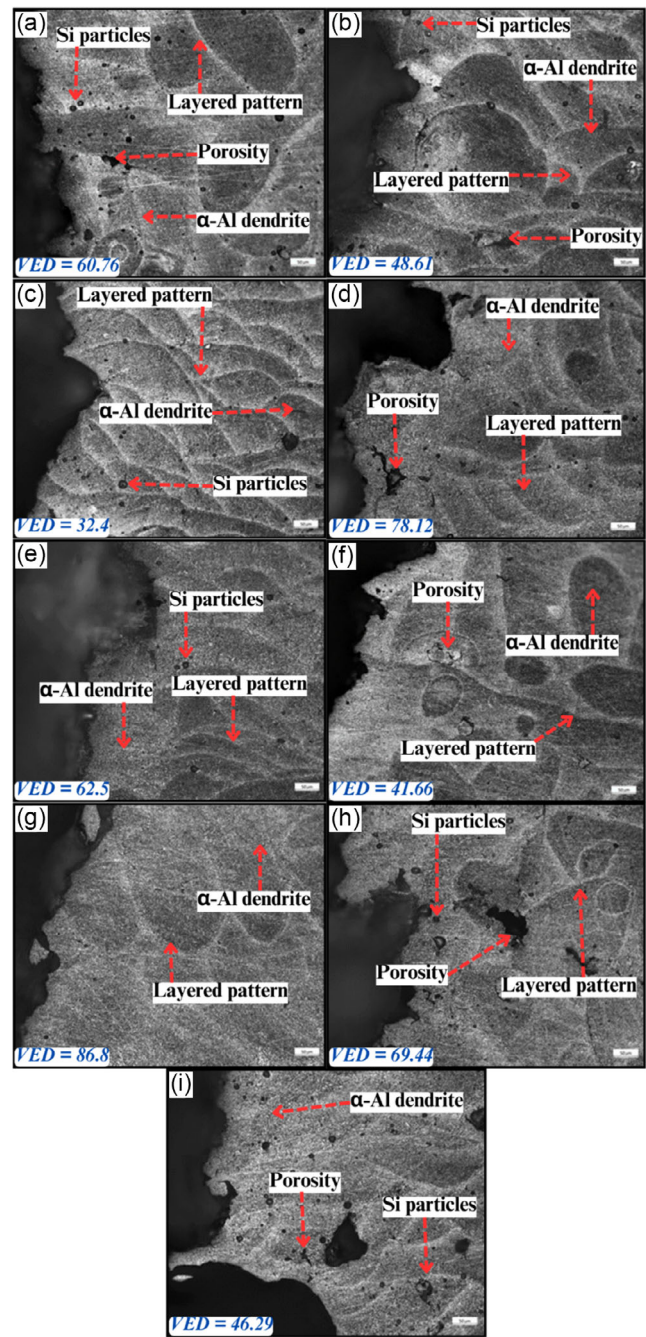


**Figure 3.** a–i) Optical micrographs of heat-treated LPBFed specimens printed using various process parameters combinations.

uneven forms between the adjacent layers.<sup>[36,67]</sup> These prior results are consistent with the findings of the current analysis.

Porosity in AlSi10Mg components produced using laser powder bed fusion methods is a common occurrence caused by several elements specific to the production technology. In the process of melting and solidification in LPBF, it is possible for gasses to get entrapped inside the molten metal. As the material hardens, the trapped gas creates holes, resulting in porosity. Inadequate energy input or incorrect scanning settings might

lead to partial fusion between nearby powder particles or layers. This partial fusion might result in the formation of cavities or pores in the final portion. LPBF uses a high-powered laser to heat and combine the metal powder via melting and fusion. When the laser beam interacts with the metal surface in an unstable way, referred to as keyhole instability, it may generate gaps and pores as it traverses the material. The characteristics of the metal powder used in LPBF may have an impact on the level of porosity. The size, shape, and chemical makeup of the powder have an impact on the degree to which it can be compressed during the melting process. LPBF requires meticulous regulation of parameters such as laser power, scanning velocity, and layer depth. Fluctuations in these parameters might cause irregularities in the rates of heating and cooling, which can contribute to the formation of pores. The rapid solidification that occurs during the LPBF process may lead to the development of unfavorable microstructures, such as porosity. Applying controlled heat treatments after processing may sometimes assist in reducing these problems. The solution heat treatment used on AlSi10Mg components produced using LPBF is essential for altering their microstructure, as shown in Figure 3. The process of solution heat treatment facilitated the even dispersion of alloying elements within the microstructure by promoting their dissolution and redistribution. As a consequence, there is a more uniform dispersion of different phases, such as silicon particles, as shown in Figure 3. LPBF generally results in the formation of microstructures with a tiny grain size as a result of fast solidification.<sup>[68]</sup> The use of solution heat treatment results in either an increase or decrease in grain size, depending on the specific temperature and duration of the treatment. It enables the deliberate adjustment of grain size, resulting in improved mechanical characteristics including strength and ductility. By effectively managing the solution treatment parameters, it is feasible to successfully attain the required grain size and dispersion. The microstructure was improved and flaws were minimized using solution heat treatment followed by quenching, resulting in components that are appropriate for demanding applications. Increased VED often led to accelerated heating and solidification rates in the LPBF process. The quick solidification process resulted in the development of smaller grains in the microstructure of the printed components. The grains were further purified using a solution heat treatment after the printing process. Additionally, it is hypothesized that the presence of tiny grains enhances the mechanical characteristics of a material by reinforcing the grain boundaries. Increasing the VED has a tendency to decrease the probability of porosity and flaws in parts manufactured using LPBF technology.<sup>[69]</sup> The negative impact of porosity on mechanical characteristics is reduced by achieving improved fusing and full melting of powder particles. The process of solution heat treatment was used to enhance the compaction and remove all residual imperfections. Ultimately, the increased volumetric energy density in LPBF led to a more precise microstructure in solution heat-treated AlSi10Mg components. This was evident by the presence of smaller grains, a consistent distribution of phases, and a reduction in flaws.

In solution heat-treated specimens, in addition to the larger molten pool, it is also evident that the number of micropores increases and their size substantially rises with the increase in VED. At  $60.76 \text{ J mm}^{-3}$ , the specimen features a relatively small

number of pores, with the majority being less than tens of  $\mu\text{m}$  in size. As VED reaches  $62.50 \text{ J mm}^{-3}$ , huge spherical pores of several tens of  $\mu\text{m}$  width emerge. The specimen processed with  $86.81 \text{ J mm}^{-3}$  has huge pores up to  $100\text{--}200 \mu\text{m}$  in size, primarily found near the base of molten pools. This observation aligns with the pattern of densification variation with VEDs. In addition to the commonly understood knowledge that a huge molten pool is created at greater VED, it can be observed that increasing VED results in an increased depth-to-width proportion of the molten pool while closely examining the molten pool properties at different VEDs.<sup>[70]</sup>

Because the variation in VED significantly impacts porosity, its influence on the microstructure is less apparent. The AlSi10Mg sample exhibits an organized microstructure, featuring the melt pools located at the outermost level. The boundaries of the melt pools are determined by coarse regions that arise from a relatively inadequate cooling rate at the local level during the solidification phase. The existence of significant columnar grains, elongated in the direction of their formation, is evident in the melt pools, highlighting a distinct variation in channeling. In addition, these grains often demonstrate epitaxial development, extending over many melt pools. Each grain is composed of a coherent and linked fibrous eutectic Si that contains tiny  $\alpha\text{-Al}$  cells. The micrometric cells are around one-tenth the size of the grains and possess a comparable elongated axis. The hierarchical microstructures consist of nanosized Si precipitates, which are situated inside the  $\alpha\text{-Al}$  cells at the innermost level. They exhibit both spherical and needle-shaped forms. The occurrence of these phenomena may be ascribed to either a reduction in the solubility of Si in the  $\alpha\text{-Al}$  cells during the cooling process, or to the influence of adjacent laser scans leading to precipitation. The lack of phases containing magnesium suggests that the element is retained inside the  $\alpha\text{-Al}$  phase as a solid solution. XRD examinations further validated the presence of a nonequilibrium microstructure as revealed by OM studies. Based on the results, a very few of the experimental peaks corresponded to a compound containing magnesium (Mg). Thus, the simulated pattern solely takes into consideration the aluminum and silicon phases (Figure 4). Contrary to the Al peak being the most prominent in the diffraction pattern, there is a distinct crystallographic texture, where the aluminum reflection is the most intense. In addition, the Si reflections in Figure 4 are hardly distinguishable from the background, indicating a lower quantity of crystalline Si with a manometer-scale size.<sup>[65]</sup> Aluminum often displayed prominent peaks at about  $2\theta$  values of  $38.3$ ,  $44.5$ , and  $65.0^\circ$  in the XRD pattern. These peaks corresponded to the (111), (200), and (220) planes, respectively, of the face-centered-cubic (FCC) crystal structure of aluminum. The (111) and (220) planes of the FCC structure of silicon were seen at  $2\theta$  values of  $28.4$  and  $47.3^\circ$ , respectively, indicating the presence of silicon peaks. The presence of magnesium in the alloy may not always be easily identifiable by distinct peaks since its concentration is lower in comparison with that of aluminum and silicon. Nevertheless, it is found in substantial quantities and has faint peaks at  $2\theta$  values that resemble those of aluminum.<sup>[71]</sup> As shown in Figure 4, the pattern of the heat-treated AlSi10Mg has more intense peaks as compared to the as-built structure, which reveals less residual stress due to the recovery and recrystallization. Peak intensities of the  $\text{Mg}_2\text{Si}$  phase are typically reduced during heat

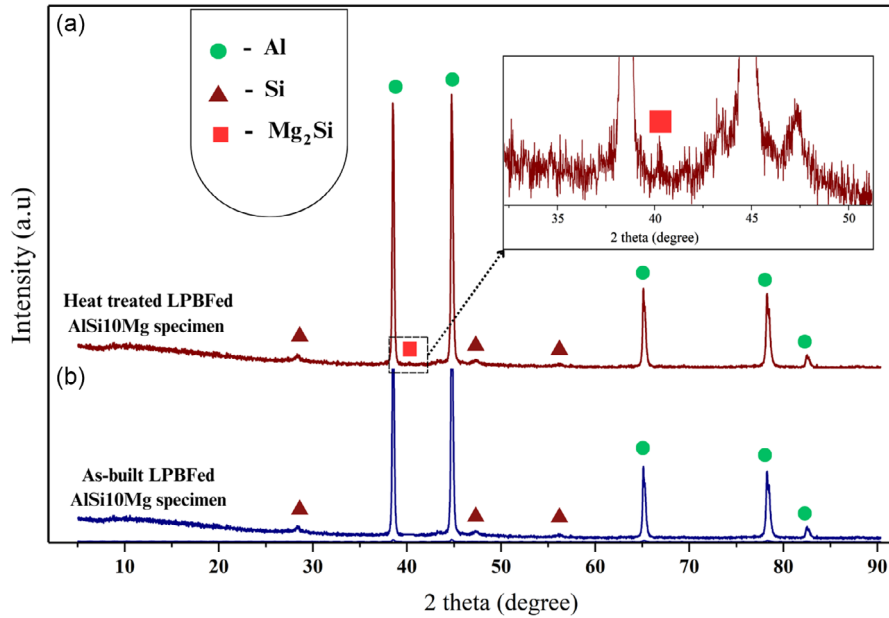


**Figure 4.** XRD spectra of LPBFed AlSi10Mg specimens a) heat-treated condition and b) as-built condition.

treatment to signify dissolution of magnesium into the Al matrix. The (222) plane associated with the formation of  $Mg_2Si$  peak observed at  $42.7^\circ$  of the diffraction angle. Nevertheless, the peak intensity is small due to the presence of a minimal 0.35 wt% of Mg. The aforementioned results are evident in the enhanced pattern of the heat-treated specimen shown in Figure 4. In more detail, an overall less remarkable peak intensity is observed, and a more equal distribution may point to a more homogeneous microstructure.

### 3.3. Tensile Strength Observations

**Table 3** displays the tensile characteristics of AlSi10Mg specimens that have been manufactured with different VEDs. **Figure 5** contains comprehensive details on various samples of VED and their associated tensile characteristics of as-built specimens. The YS reaches a maximum value of  $326.86 \text{ N mm}^{-2}$  at

the highest volumetric energy density of  $86.81 \text{ J mm}^{-3}$ . The YS exhibits a gradual linear decline, reaching a minimum value of  $278.03 \text{ N mm}^{-2}$  when the VED reduces to  $60.76 \text{ J mm}^{-3}$ . The UTS drops as the VED lowers, but the percentage of elongation increases as the VED reduces. The UTS decreases from  $326.86$  to  $278.03 \text{ N mm}^{-2}$ , while the percentage of elongation increases from 1.5% to 2.88%.

**Figure 6** contains comprehensive details on various specimens of VED and their associated tensile characteristics after heat treatment process. After heat treatment, specimens with higher VED demonstrate a decreased YS of  $267.38 \text{ N mm}^{-2}$ . Conversely, when the VED lowers, there is a significant increase in YS, reaching  $302.39 \text{ N mm}^{-2}$ . Similarly, UTS reduces from  $342.98$  to  $267.38 \text{ N mm}^{-2}$  as the VED increases. In contrast, percentage of elongation increases from 1.56% to 2.33% with an increase in VED. **Figure 7** illustrates the observed decrease in surface area of both the original and heat-treated specimens,

**Table 3.** LPBF processing parameters used and their respective experimental responses observed.

Designation	VED [ $\text{J mm}^{-3}$ ]	As-built UTS [ $\text{N mm}^{-2}$ ]	As-built YS [ $\text{N mm}^{-2}$ ]	As-built (percentage of elongation)	As-built (percentage of reduction in area)	Heat-treated UTS [ $\text{N mm}^{-2}$ ]	Heat-treated YS [ $\text{N mm}^{-2}$ ]	Heat-treated (percentage of elongation)	Heat-treated (percentage of reduction in area)
A	60.76	331.54	278.03	1.5	16.24	342.98	302.39	1.56	1.989
B	48.61	336.52	282.2	0.63	1.979	322.24	274.18	2.12	2.443
C	32.41	319.08	276.58	3.56	2.508	317.5	294.88	2.12	4.446
D	78.13	269.45	238.25	3.94	2.443	297.82	274.18	2.44	2.916
E	62.50	283.3	253.06	3.37	1.989	291.75	250.88	2.63	3.432
F	41.67	281.44	266	3.25	2.978	318.31	295.5	2.37	3.009
G	86.81	347.6	326.86	2.88	1.504	267.38	239.69	2.33	3.023
H	69.44	284.11	244.05	2	2.95	297.03	280.8	2.69	3.467
I	46.30	330.91	290.25	1.81	1.97	322.14	258.96	2.88	5.357



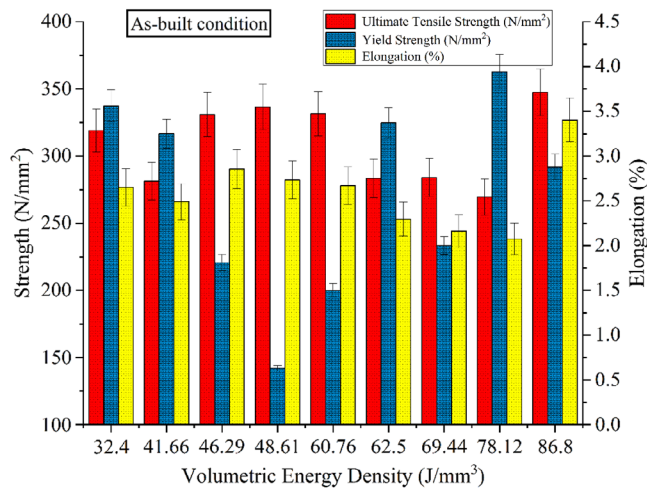


**Figure 5.** Volumetric energy density observed versus tensile properties of AlSi10Mg specimens (as-built condition).

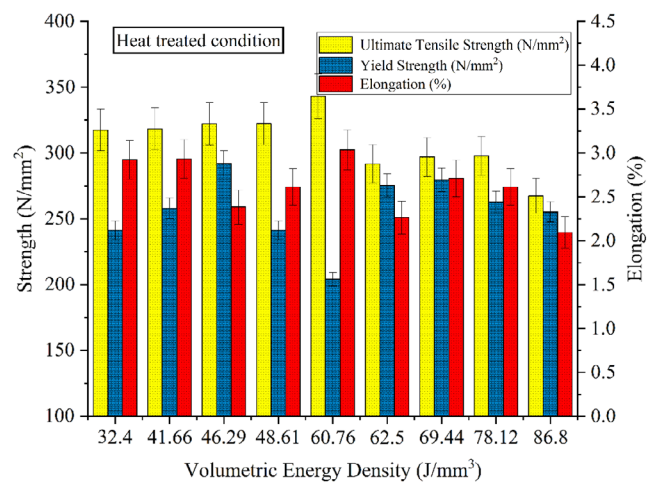


**Figure 6.** Volumetric energy density observed versus tensile properties of AlSi10Mg specimens (heat-treated condition).

indicating that heat treatment mostly reduces surface area by reducing the number of pores. The reduction in area is an important mechanical property that describes the ductility or deformation capability of a material after undergoing plastic deformation, typically due to tensile testing. LPBF printed AlSi10Mg specimens generally exhibit good ductility and deformation capabilities, reflected in a significant reduction in area during tensile testing. A significant decrease in area (5.357%) is found after subjecting the heat-treated specimen to a volumetric energy density of 46.29 J mm<sup>-3</sup>. It is hypothesized that the precipitates or secondary phases that are generated during LPBF printing are dissolved by the solution heat treatment, resulting in a more uniform structure. This enhancement resulted in an increase in the material's ability to deform without breaking and its resistance to fracture, which might possibly lead to a greater decrease in cross-sectional area. The ductility of AlSi10Mg was improved using solution heat treatment, which reduced the occurrence of brittle

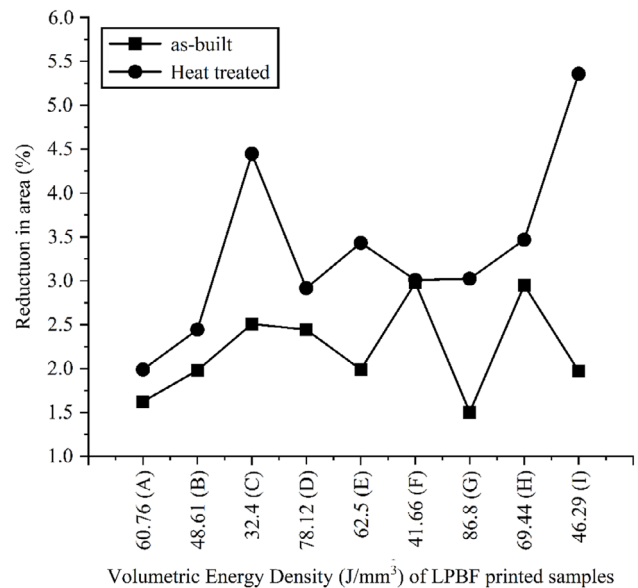


**Figure 7.** Volumetric energy density observed versus reduction in area of LPBF printed AlSi10Mg specimens.

phases and boosted the material's plastic deformation capability. The enhanced ductility is seen in the increased area reduction observed during tensile testing. Solution heat treatment is also effective in alleviating residual strains that may exist in LPBF printed components as a result of the fast thermal fluctuations experienced during the printing process. The enhanced tensile qualities, such as increased area reduction, were a result of decreased residual stresses.

### 3.4. Tensile Fractography

When AlSi10Mg alloy undergoes tensile fracture, several key factors come into play, shaping the fracture morphology and characteristics. The fractured area of as-built AlSi10Mg often displays a mixture of ductile and brittle characteristics (Figure 8a). Ductile regions often manifest as dimples or cup-like features, indicating plastic deformation prior to fracture, which is typical of metallic materials. These regions result from the movement of dislocations and the redistribution of stress during deformation. However, alongside these ductile features, one may also observe regions of brittle fracture, characterized by cleavage facets or smooth, flat surfaces. These brittle regions are often associated with the presence of defects such as pores, inclusions, or inter-metallic phases, which function as locations of high stress concentration, which encourage the development of cracks and propagation.<sup>[72]</sup> The specific distribution and interplay of ductile and brittle features on the fracture surface depend on various factors including alloy composition, processing history, loading conditions, and the presence of microstructural defects, emphasizing the importance of thorough analysis to understand the fracture behavior and improve the mechanical performance of AlSi10Mg components. The process of heat treatment is of utmost importance in determining the occurrence of tensile fracture behavior of AlSi10Mg fabricated by LPBF. As-fabricated

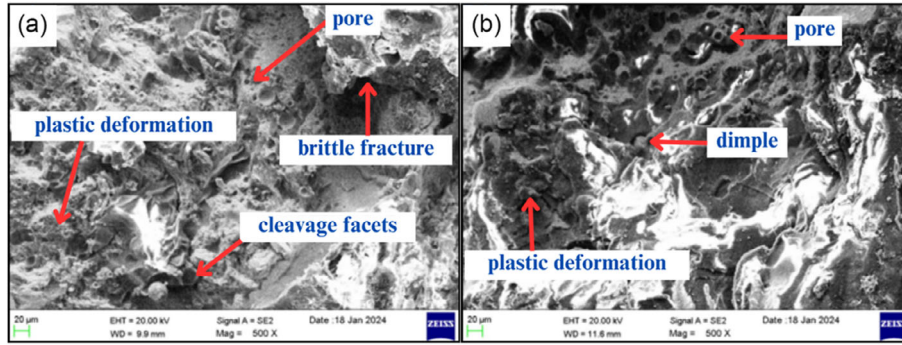


**Figure 8.** Tensile fracture surface of a) as-built specimen (H) and b) heat-treated specimen (H) having volumetric energy density of  $69.44 \text{ J mm}^{-3}$ .

AlSi10Mg parts typically exhibit a combination of microstructural features such as columnar grains, residual stresses, and potentially the existence of imperfections such as pores or non-equilibrium phases, all of which can affect mechanical properties including tensile strength and ductility. Heat treatment processes such as solutionizing and quenching can help mitigate these effects by promoting microstructural homogenization, relieving residual stresses, and enhancing the precipitation of strengthening phases.<sup>[73]</sup> Solution treatment at elevated temperatures dissolves and redistributes solute atoms, promoting grain refinement and reducing segregation, while subsequent aging treatments encourage the precipitation of strengthening phases like  $\text{Mg}_2\text{Si}$ . These heat treatment steps can lead to improvements in tensile strength and ductility by optimizing the microstructure and reducing the susceptibility to defects, ultimately influencing the fracture behavior and enhancing the mechanical performance of LPBF-fabricated AlSi10Mg components (Figure 8b).

### 3.5. Validation of Responses

**Table 4** presents comparison between the predicted value and experimental value of responses including UTS, YS, elongation (%), and reduction in area (%) of both as-built and heat-treated AlSi10Mg parts investigated in this research. First of all, these validation results show a good correlation between the

experimental and the Taguchi analysis results. This means that the orthogonal array successfully provided the interaction between LPBF processing parameters and the tensile properties. The observed errors not more than 5% ranges are notable since they are within acceptable industrial tolerances and the Taguchi methods of process improvement have thus been deemed effective.<sup>[74]</sup> The research focuses on volumetric energy density, which has a very strong impact on the microstructure and mechanical characteristics of LPBFed parts. Improvement of this parameter might improve the tensile characteristics of AlSi10Mg parts. The research findings suggest that it is possible to increase production efficiency, and that the optimization of properties and factory product performance is possible. The findings have important applications to industries that employ LPBF such as space, automobile, and biomedical field due to the importance of improved quality of printed parts. In conclusion, the study confirms the experimentally observed responses with Taguchi optimization method for predicting mechanical properties, emphasizing its feasibility in actual manufacturing conditions. The current study can be extended in the future by investigating other parameters during the processing techniques or integrating a variety of parameters to optimize the fabrication process, as well as diversifying the materials and techniques involved in the production of AlSi10Mg alloy. This research adds to the body of knowledge of AM that will enhance future production planning and strategies.

**Table 4.** Experimental values and predicted values of responses.

Responses	Optimum LPBF processing parameters with level			Predicted values of responses	Experimental values of responses	Error [%]
	Laser power [W]	Exposure time [ $\mu\text{s}$ ]	Hatch distance [mm]			
As-built UTS [ $\text{N mm}^{-2}$ ]	350	50	0.08	330	331.54	0.465
As-built YS [ $\text{N mm}^{-2}$ ]	500	50	0.08	325	326.86	0.569
As-built (percentage of elongation)	450	40	0.12	3.28	3.25	0.923
As-built (percentage of reduction in area)	350	50	0.08	15.68	16.240	3.448
Heat-treated UTS [ $\text{N mm}^{-2}$ ]	350	40	0.12	315.7	317.5	0.567
Heat-treated YS [ $\text{N mm}^{-2}$ ]	350	40	0.12	296	294.88	0.379
Heat-treated (percentage of elongation)	500	45	0.09	2.58	2.69	4.08
Heat-treated (percentage of reduction in area)	500	40	0.12	5.47	5.357	2.11



## 4. Conclusions

The current study utilized various combinations of fabrication parameters to manufacture specimens of AlSi10Mg alloy using LPBF technology. An investigation was carried out to study the impact of volumetric energy density and processing parameters on the microstructural characteristics and tensile properties of LPBFed AlSi10Mg specimens. This involved conducting metallurgical and tensile characterizations. The important findings are as follows: 1) A limited range of process parameters has a substantial influence on the porosity of the alloy, but has less impact on the microstructural properties. This is a scenario in which the process is being enhanced to minimize faults or optimize productivity. 2) The material, which is nearly dense, exhibits exceptional tensile qualities. An estimation was made to determine the individual impact of each microstructural feature on the strength of the material. The results demonstrate a strong correlation between the experimental tensile characteristics and the Al cells and Si precipitates, indicating that these factors are the main sources of reinforcement. Nevertheless, even a small amount of porosity significantly diminishes the strength of the material and surpasses the influence of its microstructure. 3) In the as-built specimen, the YS and UTS improve as the VED increases. However, the percentage elongation decreases in a consecutive manner. 4) Similarly in heat-treated specimens as the VED increases, both the YS and UTS exhibit a declining trend, while the percentage elongation shows a growing trend. The experimental findings obtained are corroborated by the predicted responses. 5) Investigating the impact of VED on AlSi10Mg alloy produced by LPBF not only improves knowledge but also facilitates progress in AM technology, material science, and industrial applications in many industries. Future research should strive to integrate theoretical insights with actual execution, therefore fostering innovation and enhancing competitiveness in AM technology.

## Acknowledgements

The authors would like to thank the Director, Dy Director Administration, and Head of department for providing timely guidance and support throughout this work. Authors extend heartfelt thanks to Mr. Amit Aware, Director & CEO, Amison Engineering, Pune, India for providing the facility and his keen interest in research. Authors extend heartfelt thanks to Ms. RohiniAvhad, Project Manager Amison Engineering, Pune, India for technical support throughout the project. Financial support for this study was provided by a grant with grant no. SIU/SCRI/MJRP-Approval/2023/1754 dated March 29, 2023 from the Symbiosis International (Deemed University), Pune, India.

## Conflict of Interest

The authors declare no conflict of interest.

## Author Contributions

**Vijaykumar S. Jatti:** conceptualization (equal); data curation (lead); formal analysis (equal); funding acquisition (lead); methodology (equal); resources (lead); validation (lead); writing—original draft (equal); writing—review and editing (equal). **A. Saiyathibrahim:** formal analysis

(lead); investigation (equal); methodology (equal); resources (equal); validation (equal); writing—original draft (equal); writing—review and editing (equal). **R. Murali Krishnan:** data curation (equal); methodology (equal); resources (supporting); validation (equal); writing—original draft (equal). **Ashwini V. Jatti:** conceptualization (equal); data curation (equal); investigation (equal); methodology (equal); project administration (equal); visualization (equal); writing—review and editing (equal). **G. Suganya Priyadharshini:** investigation (equal); methodology (supporting); project administration (equal); resources (supporting); validation (equal); writing—original draft (equal). **Dhanesh G. Mohan:** conceptualization (lead); data curation (equal); formal analysis (lead); methodology (lead); project administration (lead); supervision (lead); validation (equal); writing—review and editing (equal). Further, all authors read and approved the final manuscript.

## Data Availability Statement

All necessary data are shown in the figures and tables within the document. The raw data can be made available upon request.

## Keywords

AlSi10Mg, heat treatment, laser powder bed fusion, tensile fractography, tensile strength, volumetric energy density

Received: August 13, 2024

Revised: September 30, 2024

Published online:

- [1] J. R. Díaz-Reza, J. R. Mendoza-Fong, J. Blanco-Fernández, J. A. Marmolejo-Saucedo, J. L. García-Alcaraz, *Appl. Sci.* **2019**, *9*, 3741.
- [2] R. Citarella, V. Giannella, *Appl. Sci.* **2021**, *11*, 840.
- [3] A. Vafadar, F. Guzzomi, A. Rassau, K. Hayward, *Appl. Sci.* **2021**, *11*, 1213.
- [4] M. Q. Zafar, H. Zhao, *Met. Mater. Int.* **2020**, *26*, 564.
- [5] S. Rouf, A. Malik, N. Singh, A. Raina, N. Naveed, M. I. H. Siddiqui, M. I. U. Haq, *Sustainable Oper. Comput.* **2022**, *3*, 258.
- [6] S. Cooke, K. Ahmadi, S. Willerth, R. Herring, *J. Manuf. Processes* **2020**, *57*, 978.
- [7] O. D. Neikov, *Handbook of Non-Ferrous Metal Powders*, Vol. 2, **2019**, p. 373–399.
- [8] M. Armstrong, H. Mehrabi, N. Naveed, *J. Manuf. Processes* **2022**, *84*, 1001.
- [9] Metal AM Parts in Series Production for BMW's New i8 Roadster <https://www.metal-am.com/metal-parts-series-production-bmw-new-i8-roadster/> (accessed: December 2017).
- [10] J. Karimi, C. Suryanarayana, I. Okulov, K. G. Prashanth, *Mater. Sci. Eng., A* **2021**, *805*, 140558.
- [11] C. Zhang, H. Zhu, Z. Hu, L. Zhang, X. Zeng, *Mater. Sci. Eng., A* **2019**, *746*, 416.
- [12] Y. Deng, Z. Mao, N. Yang, X. Niu, X. Lu, *Materials* **2020**, *13*, 1601.
- [13] S. Zhang, H. Zhu, Z. Hu, X. Zeng, F. Zhong, *Powder Technol.* **2019**, *342*, 613.
- [14] E. M. Sefene, *J. Manuf. Syst.* **2022**, *63*, 250.
- [15] H. Qin, Q. Dong, V. Fallah, M. R. Daymond, *Metall. Mater. Trans. A* **2020**, *51*, 448.
- [16] Q. Dong, A. Howells, D. J. Lloyd, M. Gallerneault, V. Fallah, *Mater. Sci. Eng., A* **2020**, *772*, 138693.
- [17] M. Ghasri-Khouzani, H. Peng, R. Attardo, P. Ostiguy, J. Neidig, R. Billo, M. R. Shankar, *J. Manuf. Processes* **2019**, *37*, 274.

- [18] K. DePalma, M. R. Walluk, A. Murtaugh, J. Hilton, S. McConky, B. Hilton, *J. Cleaner Prod.* **2020**, *264*, 121567.
- [19] J. Zhang, B. Song, Q. Wei, D. Bourell, Y. Shi, *J. Mater. Sci. Technol.* **2019**, *35*, 270.
- [20] P. Gradl, D. C. Tinker, A. Park, O. R. Mireles, M. Garcia, R. Wilkerson, C. Mckinney, *J. Mater. Eng. Perform.* **2022**, *31*, 6013.
- [21] P. Li, F. Xu, S. Robertson, Z. Zhou, X. Hou, A. T. Clare, N. T. Aboulkhair, *Mater. Des.* **2022**, *216*, 110543.
- [22] J. Liu, P. Wen, *Mater. Des.* **2022**, *215*, 110505.
- [23] Z. W. Xu, Q. Wang, X. S. Wang, C. H. Tan, M. H. Guo, P. B. Gao, *Mech. Mater.* **2020**, *148*, 103499.
- [24] W. Zhang, Y. Hu, X. Ma, G. Qian, J. Zhang, Z. Yang, F. Berto, *Int. J. Fatigue* **2021**, *145*, 106109.
- [25] H. Hyer, L. Zhou, S. Park, G. Gottsfrizt, G. Benson, B. Tolentino, Y. Sohn, *Metall. Microstruct. Anal.* **2020**, *9*, 484.
- [26] N. T. Aboulkhair, M. Simonelli, L. Parry, I. Ashcroft, C. Tuck, R. Hague, *Prog. Mater. Sci.* **2019**, *106*, 100578.
- [27] Z. Wang, R. Ummethala, N. Singh, S. Tang, C. Suryanarayana, J. Eckert, K. G. Prashanth, *Materials* **2020**, *13*, 4564.
- [28] P. Ansari, M. U. Salamci, *J. Alloys Compd.* **2022**, *890*, 161873.
- [29] M. A. Pekok, R. Setchi, M. Ryan, Q. Han, D. Gu, *Int. J. Adv. Manuf. Technol.* **2021**, *112*, 175.
- [30] T. Kimura, T. Nakamoto, T. Ozaki, K. Sugita, M. Mizuno, H. Araki, *Mater. Sci. Eng., A* **2019**, *754*, 786.
- [31] E. Sert, L. Hitzler, S. Hafenstein, M. Merkel, E. Werner, A. Öchsner, *Prog. Addit. Manuf.* **2020**, *5*, 305.
- [32] J. Guan, Y. Jiang, X. Zhang, X. Chong, *Mater. Charact.* **2020**, *161*, 110079.
- [33] B. Liu, B. Q. Li, Z. Li, *Results Phys.* **2019**, *12*, 982.
- [34] M. Gandolfi, M. G. C. Xavier, L. F. Gomes, R. A. V. Reyes, A. Garcia, J. E. Spinelli, *Metals* **2021**, *11*, 1019.
- [35] T. Hirata, T. Kimura, T. Nakamoto, *Mater. Sci. Eng., A* **2020**, *772*, 138713.
- [36] N. Limbasiya, A. Jain, H. Soni, V. Wankhede, G. Krolczyk, P. Sahlot, *J. Mater. Res. Technol.* **2022**, *667*, 139.
- [37] Z. Liu, J. Sun, Z. Yan, Y. Lin, M. Liu, H. J. Roven, A. K. Dahle, *Mater. Sci. Eng., A* **2021**, *806*, 140806.
- [38] C. Gao, W. Wu, J. Shi, Z. Xiao, A. H. Akbarzadeh, *Addit. Manuf.* **2020**, *34*, 101378.
- [39] H. Wu, Y. Ren, J. Ren, L. Liang, R. Li, Q. Fang, I. Baker, *J. Alloys Compd.* **2021**, *873*, 159823.
- [40] T. H. Park, M. S. Baek, H. Hyer, Y. Sohn, K. A. Lee, *Mater. Charact.* **2021**, *176*, 111113.
- [41] J. Jakumeit, G. Zheng, R. Laqua, S. J. Clark, J. Zielinski, J. H. Schleifenbaum, P. D. Lee, *Addit. Manuf.* **2021**, *47*, 102332.
- [42] L. Tonelli, A. Fortunato, L. Ceschini, *J. Manuf. Processes* **2020**, *52*, 106.
- [43] A. Kempf, K. Hilgenberg, *Mater. Sci. Eng., A* **2020**, *776*, 138976.
- [44] Z. H. Li, Y. F. Nie, B. Liu, Z. Z. Kuai, M. Zhao, F. Liu, *Mater. Des.* **2020**, *192*, 108709.
- [45] K. Riemer, N. Albrecht, S. Ziegelmeier, R. Ramakrishnan, L. Haferkamp, A. B. Spierings, G. J. Leichtfried, *Addit. Manuf.* **2020**, *34*, 101286.
- [46] B. Blakey-Milner, P. Gradl, G. Snedden, M. Brooks, J. Pitot, E. Lopez, M. Leary, F. Berto, A. Du Plessis, *Mater. Des.* **2021**, *209*, 110008.
- [47] N. Diaz Vallejo, C. Lucas, N. Ayers, K. Graydon, H. Hyer, Y. Sohn, *Metals* **2021**, *11*, 832.
- [48] F. Caiazza, V. Alfieri, G. Casalino, *Materials* **2020**, *13*, 538.
- [49] M. Giovagnoli, G. Silvi, M. Merlin, M. T. Di Giovanni, *Mater. Sci. Eng., A* **2021**, *802*, 140613.
- [50] A. K. Singla, M. Banerjee, A. Sharma, J. Singh, A. Bansal, M. K. Gupta, N. Khanna, A. S. Shahi, D. K. Goyal, *J. Manuf. Processes* **2021**, *64*, 161.
- [51] C. Garcia-Cabazon, M. A. Castro-Sastre, A. I. Fernandez-Abia, M. L. Rodriguez-Mendez, F. Martin-Pedrosa, *Met. Mater. Int.* **2022**, *28*, 2652.
- [52] E. Padovano, C. Badini, A. Pantarelli, F. Gili, F. D'Aiuto, *J. Alloys Compd.* **2020**, *831*, 154822.
- [53] T. DebRoy, T. Mukherjee, J. O. Milewski, J. W. Elmer, B. Ribic, J. J. Blecher, W. Zhang, *Nat. Mater.* **2019**, *18*, 1026.
- [54] M. Cabrini, F. Calignano, P. Fino, S. Lorenzi, M. Lorusso, D. Manfredi, T. Pastore, *Materials* **2018**, *11*, 1051.
- [55] M. Liu, N. Takata, A. Suzuki, M. Kobashi, *Materials* **2020**, *13*, 2487.
- [56] K. Moefar, F. Khodabakhshi, S. F. Kashani-Bozorg, M. Mohammadi, A. P. Gerlich, *J. Mater. Res. Technol.* **2022**, *16*, 1029.
- [57] V. Mercurio, F. Calignano, L. Iuliano, *Int. J. Adv. Manuf. Technol.* **2023**, *125*, 3117.
- [58] Z. Dong, M. Xu, H. Guo, X. Fei, Y. Liu, B. Gong, G. Ju, *J. Mater. Res. Technol.* **2022**, *17*, 2343.
- [59] A. Salandari-Rabori, P. Wang, Q. Dong, V. Fallah, *Mater. Sci. Eng., A* **2021**, *805*, 140620.
- [60] R. Zhao, C. Chen, W. Wang, T. Cao, S. Shuai, S. Xu, Z. Ren, *Addit. Manuf.* **2022**, *51*, 102605.
- [61] M. A. Mahmood, A. C. Popescu, M. Oane, C. Ristoscu, D. Chioibasu, S. Mihai, I. N. Mihailescu, *Metals* **2020**, *10*, 1113.
- [62] J. H. Zhou, *J. Phys.:Conf. Ser.* **2020**, *1634*, 012103.
- [63] T. Yang, T. Liu, W. Liao, E. MacDonald, H. Wei, C. Zhang, K. Zhang, *J. Alloys Compd.* **2020**, *849*, 156300.
- [64] M. Liu, K. Wei, R. Zhou, X. Yue, X. Zeng, *Virtual Phys. Prototyping* **2022**, *17*, 749.
- [65] Y. Cao, X. Lin, Q. Z. Wang, S. Q. Shi, L. Ma, N. Kang, W. D. Huang, *J. Mater. Sci. Technol.* **2021**, *62*, 162.
- [66] V. M. R. Santos, A. Thompson, D. Sims-Waterhouse, I. Maskery, P. Woolliams, R. Leach, *Addit. Manuf.* **2020**, *32*, 100964.
- [67] M. P. Behera, T. Dougherty, S. Singamneni, K. De Silva, *Mater. Today: Proc.* **2020**, *33*, 5729.
- [68] C. Guo, S. Li, S. Shi, X. Li, X. Hu, Q. Zhu, R. M. Ward, *J. Mater. Process. Technol.* **2020**, *285*, 116788.
- [69] P. Köhnen, S. Ewald, J. H. Schleifenbaum, A. Belyakov, C. Haase, *Addit. Manuf.* **2020**, *35*, 101389.
- [70] J. Elambasseril, J. Rogers, C. Wallbrink, D. Munk, M. Leary, M. Qian, *Crit. Rev. Solid State Mater. Sci.* **2023**, *48*, 132.
- [71] Y. S. Eom, J. M. Park, J. W. Choi, D. J. Seong, H. Joo, Y. C. Jo, I. Son, *J. Alloys Compd.* **2023**, *956*, 170348.
- [72] P. Wang, A. Salandari-Rabori, Q. Dong, V. Fallah, *J. Manuf. Processes* **2021**, *64*, 633.
- [73] P. Angolkar, M. M. Hussain, *Tribol. Ind.* **2023**, *45*, 561.
- [74] W. L. Oberkampf, M. F. Barone, *J. Comput. Phys.* **2006**, *217*, 5.